Spectral integral representations of monostatic backscattering from three-dimensional distributions of sediment volume inhomogeneities

Kevin D. LePage
SACLANT Undersea Research Centre, I-19138 La Spezia, Italy

Henrik Schmidt
Massachusetts Institute of Technology, Cambridge, Massachusetts 02139

(Received 1 May 2002; revised 17 August 2002; accepted 15 September 2002)

A theory is developed for generating short time, monostatic reverberation realizations caused by three-dimensionally distributed volume inhomogeneities in stratified media. A wave number integral approach to treating the propagation to and from the scatterers, combined with a two-dimensional spectral representation of the azimuthally averaged scatterer realizations and a novel numerical implementation, combine to yield an efficient, high fidelity reverberation simulator for predicting monostatic backscatter from horizontally stratified sediments. © *2003 Acoustical Society of America.* [DOI: 10.1121/1.1528625]

PACS numbers: 43.30.Bp, 43.30.Gv, 43.30.Hw [WMC]

I. INTRODUCTION

The prediction of scattering from sediment volume inhomogeneities has been the subject of extensive study over the years.[1–13] Typically the sediment is treated as a homogeneous medium in which small perturbations in sound speed and density are superimposed. Due to the nature of the problem, predictions of scattered intensity are usually obtained under one or more subsequent approximations. When propagation is treated with a full wave approach, the perturbations are usually assumed to be uncorrelated vertically in order to obtain closed from expressions for the expected value of scattered intensity.[3,5] If the propagation is simplified under the assumption that the scatterers are excited only by propagating waves, scattered intensity may also be obtained in closed form.[6,7] If the interaction of the field with the scatterers is asymptotically evaluated, the full scattering of propagating and inhomogeneous waves may be evaluated for three-dimensional distributions of scatterers, away from the part of the sediment ensonified near the critical angle.[9,10] However, if the propagation is to be treated ''exactly'' and a three-dimensional distribution of scatterers is to be retained, then Monte Carlo techniques for estimating the scattered intensity caused by sediment volume inhomogeneities are required. In a previous paper the authors laid out the theoretical basis for a unified treatment of sediment volume inhomogeneity scattering using spectral techniques.[11] In that paper the treatment of scattering from sound speed and density inhomogeneity scattering in general horizontally stratified acoustic media, including stratifications with background sound speed gradients, was presented for the two-dimensional wave equation. While this development was useful for understanding some of the behaviors of sediment scattering in refractive layered media, the results themselves cannot be used directly to interpret data because of the 2-D geometry used. We have therefore been motivated to extend the wave number integral approach to treat laterally monostatic scattering in three dimensions, which we view as a crucial step in extending the utility of the model.

Three-dimensional scattering under the perturbation approximation is theoretically very similar to the two-dimensional problem, especially in the fundamental equations. However the implementation is more computationally demanding. The wave number integrals which must be evaluated for three-dimensional problems are Hankel transforms rather than Fourier transforms. For bistatic problems there is the requirement to evaluate $k_o r$ Fourier orders n, where r is the bistatic separation between the source and the receiver, and k_o is the background sound speed.[14,15] Finally, there is potentially a much larger number of contributing scatterers to be summed over to give the backscattered pressure, due to the addition of a dimension. For these reasons the generation of wave theoretic scattered field predictions for general bistatic geometries and scatterer distributions is a computationally demanding area which is just beginning to be explored.[12,14]

In this paper we take the first step toward a general three-dimensional wave theoretic scatter prediction capability. We show that simplified expressions for backscatter may be obtained for laterally monostatic scenarios with horizontally isotropically distributed sediment inhomogeneities. In these cases the wave number integral representation of scattering from three-dimensional sound speed fluctuations may still be obtained with one-dimensional integral transforms. The result is that a high fidelity computational capability for the generation of backscattering time series is obtained for relatively small cost over the previous two-dimensional implementation. Since the results are wave theoretic, the propagation is treated properly for general stratified acoustic media, including the presence of background sound speed gradients. Propagation near the critical angle is accurately calculated for fast sediments, and propagation near turning points is accurately calculated for refractive sediments. And since the distribution properties of the inhomogeneities of

the scatterers are intrinsically three dimensional, scattering from realistic scatterer distributions may be evaluated. The combination of these two factors and a unique numerical implementation introduces a new prediction capability into the field of sediment acoustics.

II. THEORY

The first order scattered pressure observed at the field point $\{x, y, z\}$ due to small perturbation volume inhomogeneity scattering from sound speed perturbations $\Delta c/c$ in the depth interval $[z_1, z_2]$ is given by the convolution integral[11]

$$p_s(x,y,z) = 2k_b^2 \int_{-\infty}^{\infty} dx' \int_{-\infty}^{\infty} dy' \int_{z_1}^{z_2} dz' G(\mathbf{r},\mathbf{r}') \times \frac{\Delta c}{c}(x',y',z') p(x',y',z'), \tag{1}$$

where under the Born Approximation, p is the pressure incident on the scatterers in the absence of scattering effects, $G(\mathbf{r},\mathbf{r}')$ is the Green function from the scatterer at $\mathbf{r}' = (x',y',z')$ to the observer at $\mathbf{r} = (x,y,z)$, and the three-dimensional integral integrates over the space of contributing scatterers $\Delta c/c$. In a wave number integral modeling framework for an axisymmetric horizontally stratified medium, the Green function has the wave number integral representation[16]

$$G(R,z,z') = \int_0^{\infty} g(q_r;z,z') J_0(Rq_r) q_r \, dq_r, \tag{2}$$

with $R = |\mathbf{r} - \mathbf{r}'| = \sqrt{(x-x')^2 + (y-y')^2}$ representing the horizontal separation of scatterer and observer. $g(q_r;z,z')$ is the *depth-separated Green function* which, for example, in the case of a homogeneous background medium with acoustic wave number k_0, is[17]

$$g(q_r;z,z') = \frac{i}{4\pi} \frac{e^{i|z-z'|\sqrt{k_o^2 - q_r^2}}}{\sqrt{k_o^2 - q_r^2}}. \tag{3}$$

Similarly, for scatterers in a horizontally stratified ocean model, the incident acoustic pressure may be represented by a harmonic sum over Hankel transforms

$$p(x',y',z') = \sum_{n=0}^{\infty} \begin{Bmatrix} \cos n\theta' \\ \sin n\theta' \end{Bmatrix} \int_0^{\infty} \tilde{p}_n(k_r,z') J_n(k_r r') k_r \, dk_r, \tag{4}$$

where $r' \equiv \sqrt{x'^2 + y'^2}$ and $\theta' \equiv \arccos(x'/r')$.

A. Monostatic backscatter

In the case of observations of scattering in a laterally monostatic geometry $x, y \equiv 0$, Eq. (1) considerably simplifies when the source is horizontally omnidirectional. Then the only nonzero Fourier harmonic in the source expansion is $n = 0$, and upon substitution of Eqs. (2) and (4), Eq. (1) may be written

$$p_s(z) = 2k_b^2 \int_{-\infty}^{\infty} dx' \int_{-\infty}^{\infty} dy' \int_{z_1}^{z_2} dz' \frac{\Delta c}{c}(x',y',z') \times \int_0^{\infty} g(q_r;z,z') J_0(q_r r') q_r \, dq_r \times \int_0^{\infty} \tilde{p}_0(k_r,z') J_0(k_r r') k_r \, dk_r, \tag{5}$$

or equivalently, converting to cylindrical coordinates and setting $\delta c \equiv \Delta c/c$,

$$p_s(z) = 2k_b^2 \int_0^{\infty} r' dr' \int_{z_1}^{z_2} dz' \int_0^{2\pi} d\theta \, \delta c(r',\theta,z') \times \int_0^{\infty} g(q_r;z,z') J_0(q_r r') q_r \, dq_r \times \int_0^{\infty} \tilde{p}_0(k_r,z') J_0(k_r r') k_r \, dk_r. \tag{6}$$

This is not in the most efficient form for calculating scattering in a layered waveguide. This is because Eq. (6) requires an azimuthally integrated realization of the sound speed defect, which implies that a full three-dimensional realization of the defects has to be computed on a cylindrical grid, which must then be integrated over azimuth by numerical quadrature. In general, we would like to be able to generate a realization of an azimuthally integrated realization directly without having to implement the quadrature. As we show below, if we know the two-dimensional Cartesian coordinate power spectrum of the defects as a function of depth, and this spectrum is for a homogeneous, isotropic process, then it is possible to calculate the azimuthally integrated realizations directly.

We first represent the scatterer realization in cylindrical coordinates as a two dimensional Fourier transform of the Cartesian scatterer spectrum at depth z', with a change of variables to cylindrical wavenumber coordinates

$$\delta c(r',\theta,z') = \int_0^{\infty} p_r' \, dp_r' \int_0^{2\pi} d\theta' \, \tilde{\delta c}(p_r' \cos\theta', p_r' \sin\theta', z') \times e^{ip_r' r' \cos\theta' \cos\theta} e^{ip_r' r' \sin\theta' \sin\theta}. \tag{7}$$

We may then integrate δc with respect to θ by utilizing the trigonometric identity $\cos(\theta - \theta') = \cos\theta\cos\theta' + \sin\theta\sin\theta'$ and recognizing the integral representation of the Bessel function J_o. The result is

$$\begin{aligned} \int_0^{2\pi} d\theta \, \delta c(r',\theta,z') &= \int_0^{\infty} p_r' \, dp_r' \int_0^{2\pi} d\theta' \, \tilde{\delta c}(p_r' \cos\theta', p_r' \sin\theta', z') \times \int_0^{2\pi} d\theta \, e^{ip_r' r' \cos(\theta - \theta')} \\ &= 2\pi \int_0^{\infty} p_r' \, dp_r' \int_0^{2\pi} d\theta' \, \tilde{\delta c}(p_r' \cos\theta', p_r' \sin\theta', z') \times J_o(p' r'). \end{aligned} \tag{8}$$

$\tilde{\delta c}$ is the Fourier transform of a random variable conforming to a known two-dimensional power spectrum $P_{\delta c}$. If we want to know the equivalent power spectrum of the azimuthal integral of δc at wave number p_r' then we must evaluate the expected value of the square of the Hankel transform of Eq. (8)

$$\int_0^{2\pi} d\theta_1 \int_0^{2\pi} d\theta_2 \langle \delta c(p_{r1},\theta_1,z')\,\delta c(p_{r2},\theta_2,z')\rangle$$

$$= 4\pi^2 \int_0^{2\pi} d\theta_1' \int_0^{2\pi} d\theta_2' \langle \tilde{\delta c}(p_{r1}\cos\theta_1', p_{r1}\sin\theta_1', z')$$

$$\times \tilde{\delta c}(p_{r2}\cos\theta_2', p_{r2}\sin\theta_2', z')\rangle. \tag{9}$$

If δc is a homogeneous random process, such that its correlation function is a function only of $[r_1'-r_2', \theta_1-\theta_2]$, then each wave number of the power spectrum is an independent random process. In this case the ensemble average inside the integrals over θ_1' and θ_2' on the second line of Eq. (9) is

$$\langle \tilde{\delta c}(p_{r1}\cos\theta_1', p_{r1}\sin\theta_1', z')\,\tilde{\delta c}(p_{r2}\cos\theta_2', p_{r2}\sin\theta_2', z')\rangle$$

$$\equiv P_{\delta c}(p_{r1}\cos\theta_1', p_{r1}\sin\theta_1')\,\delta(p_{r1}-p_{r2})\,\frac{\delta(\theta_1'-\theta_2')}{p_{r1}}. \tag{10}$$

Furthermore, if the power spectrum is not only for a homogeneous process but also for an isotropic one, then $P_{\delta c}(p_{r1}\cos\theta_1', p_{r1}\sin\theta_1') \equiv P_{\delta c}(p_{r1})$ and the left hand size of Eq. (9) may be integrated yielding

$$\int_0^{2\pi} d\theta_1 \int_0^{2\pi} d\theta_2 \langle \delta c(p_{r1},\theta_1,z')\,\delta c(p_{r2},\theta_2,z')\rangle$$

$$= 8\pi^3 P_{\delta c}(p_{r1})\,\frac{\delta(p_{r1}-p_{r2})}{p_{r1}}. \tag{11}$$

Equation (11) is the variance of the azimuthally integrated sound speed defect δc for wave numbers p_{r1} and p_{r2} at a depth of z'. The delta function indicates that the wave number bins are uncorrelated. Thus it follows that if we want to generate realizations of $\int_0^{2\pi} d\theta\ \delta c(r,\theta,z')$ consistent with the spectral variance in Eq. (10), we need only evaluate the Hankel transform of a kernel which is an uncorrelated Normal random variable with variance $8\pi^3[P_{\delta c}(p_r)/p_r]$

$$\int_0^{2\pi} d\theta\, \delta c(r',\theta,z')$$

$$= 2\pi\sqrt{2\pi} \int_0^{\infty} dp_r \sqrt{p_r} J_o(p_r r') N(0, P_{\delta c}(p_r)). \tag{12}$$

Insertion of Eq. (12) into Eq. (6) then yields

$$p_s(z) = 4\pi\sqrt{2\pi}k_b^2 \int_0^{\infty} r'\,dr' \int_{z_1}^{z_2} dz' \int_0^{\infty} \sqrt{p_r} N(0, P_{\delta c}(p_r, z'))$$

$$\times J_0(p_r r')\,dp_r \int_0^{\infty} g(q_r; z, z') J_0(q_r r')\, q_r\, dq_r$$

$$\times \int_0^{\infty} \tilde{p}_0(k_r, z') J_0(k_r r')\, k_r\, dk_r. \tag{13}$$

Changing the orders of integration, Eq. (13) can be cast into a form which is directly suited for implementation in a wave number integration modeling framework for ocean waveguides,

$$p_s(z) = 4\pi\sqrt{2\pi}k_b^2 \int_0^{\infty} q_r\, dq_r \int_{z_1}^{z_2} dz' g(q_r; z, z')$$

$$\times \int_0^{\infty} J_0(q_r r')\, r'\, dr' \int_0^{\infty} \sqrt{p_r} N(0, P_{\delta c}(p_r, z'))$$

$$\times J_0(p_r r')\, dp_r \int_0^{\infty} \tilde{p}_0(k_r, z') J_0(k_r r')\, k_r\, dk_r. \tag{14}$$

In this form the two inner integrals are uncoupled and may be evaluated directly *a priori* for a selected grid of scatterers in the spatial (r', z') domain. The integral over k_r represents the incident pressure field, while the integral over p_r represents the cylindrically averaged scattering strength at (r', z'). The product of these integrals then represents the horizontal distribution of virtual sources at depth z' contributing to the scattered field. The Hankel transform integral over r' converts this sheet of virtual sources into an equivalent wave number spectrum, which when multiplied by the depth-dependent Green function represents the generated scattered field component at horizontal wave number q_r. The depth integral then superimposes the contributions from all scatterer depths to produce the total kernel of the Hankel transform integral for the monostatic reverberent field on the coordinate axis $r=0$, which is evaluated using any of the standard wave number integration techniques.[10]

B. Fast Hankel transform evaluation

In underwater acoustic modeling the Hankel transform wave number integrals have traditionally been evaluated using the so called Fast Field Program (FFP) approach,[18] which is based on the large argument asymptotic of the Hankel functions. However, for the bottom scattering problem this approach is inadequate because of the significance of the steep angle contributions from scatterers at short range. Even on todays computers the generation of Bessel functions is time consuming, and a direct numerical quadrature technique for evaluating the Hankel transforms in Eq. (14) is infeasible. A number of *Fast Hankel Transforms* (FHT) have been developed,[19–21] but they generally have nonuniform sampling requirements and therefore not best suited to the ocean acoustics problem where the field is desired at a predetermined grid of horizontal ranges. Being based on the Fast Fourier Transform (FFT), the advantage of the FFP is that it efficiently approximates the Hankel transform on a regular grid of wave numbers and ranges. However, it is possible to design a numerically efficient correction to the FFP which allows for accurate accounting for the small argument contributions.

The Hankel transform integrals are of the form

$$f(r) = \int_0^{\infty} f(k) k J_m(kr)\, dk$$

$$= \frac{1}{2} \int_0^{\infty} f(k) k [H_m^{(1)}(kr) + H_m^{(2)}(kr)]\, dk, \tag{15}$$

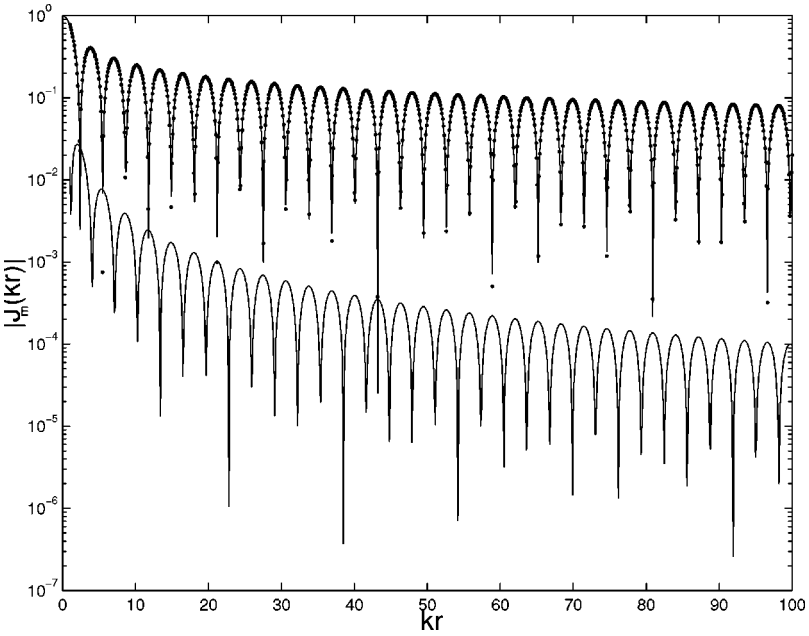

FIG. 1. Error of far-field approximation of $J_0(kr)$. Solid: Exact. Dots: Large-argument approximation. Lower curve: Error.

where $H_m^{(1)}$ for $\exp -i\omega t$ time-dependence corresponds to outgoing waves and $H_m^{(2)}$ to incoming waves, both of azimuthal Fourier order m dependence. For classical acoustic forward propagation modeling the incoming waves are ignored, eliminating the second term. However, for the backscattering problem they must be retained. We can represent the Hankel functions $H_m^{(1,2)}(k_r r)$ by their asymptotic form[22]

$$\lim_{kr\to\infty} H_m^{(1,2)}(k_r r) = \sqrt{\frac{2}{\pi k_r r}}\, e^{\pm i[k_r r-(m+1/2)\pi/2]}, \tag{16}$$

to arrive at the following approximation to the Hankel transform,

$$f^*(r) = \sqrt{\frac{1}{2\pi r}} \int_0^\infty f(k)\sqrt{k}[e^{i[kr-(m+1/2)\pi/2]} + e^{-i[kr-(m+1/2)\pi/2]}]dk. \tag{17}$$

This integral can be rewritten as a two-sided Fourier transform,

$$f^*(r) = \int_{-\infty}^{\infty} g(k) e^{ikr}\, dk, \tag{18}$$

with the kernel

$$g(k) = \begin{cases} f(-k)\sqrt{\dfrac{-k}{2\pi r}}\, e^{i(m+1/2)\pi/2} & k < 0 \\ f(k)\sqrt{\dfrac{k}{2\pi r}}\, e^{-i(m+1/2)\pi/2} & k \geqslant 0 \end{cases}. \tag{19}$$

The Fourier transform is efficiently evaluated using a standard FFT if the range r and wave number k are discretized equidistantly, with the sampling intervals being constrained by

$$\Delta r \Delta k_r = \frac{2\pi}{M}, \tag{20}$$

where M is the length of the discrete Fourier transform sequence M, which is generally a power of 2.

The error associated with using Eq. (18) is clearly associated with the approximation of the Bessel function in terms of the asymptotic expressions of the Hankel functions. Figure 1 shows the exact value of the absolute value of the Bessel function $J_0(kr)$ for $kr \leqslant 100$ as a solid curve and the asymptotic values indicated by the dots. The absolute error is indicated by the lower curve, and it is clear that the relative error of the approximation is greater than 10^{-5} for $kr \leqslant 20\pi$. Consequently, to achieve a more accurate evaluation of the Hankel transforms of order $n=0$ in Eq. (14) it is only necessary to correct the contributions corresponding values of $kr \leqslant \mathrm{KR} = 20\pi$. This is performed in a numerically stable manner by a weighted average of the contributions of the exact Bessel function and the approximate FFP kernel,

$$f(r) = f^*(r) + \int_0^\infty f(k) w(kr) k J_0(kr) dk - \int_0^\infty f(k) w(kr) \sqrt{\frac{k}{2\pi r}}[e^{i(kr-(m+1/2)\pi/2)} + e^{-i(kr-(m+1/2)\pi/2)}]dk, \tag{21}$$

where we have chosen the tapered weight function $w(kr)$ as

$$w(kr) = \begin{cases} 1 & kr \leqslant \mathrm{KR}/2 \\ [1+\cos(\pi(kr-\mathrm{KR}/2)/(\mathrm{KR}/2))]/2 & \mathrm{KR}/2 < kr < \mathrm{KR} \\ 0 & kr \geqslant \mathrm{KR} \end{cases}. \tag{22}$$

Equation (21) can be evaluated very efficiently. First of all, with the wave number and range sampling constrained by Eq. (20), all values of the exponentials are computed as part of the FFT evaluation of Eq. (17). Second, the Bessel func-

tions will only be needed for a limited number of discrete values of the argument,

$$kr = n\Delta k \Delta r, \quad n = 0,...,\mathrm{KR}/(\Delta k \Delta r), \tag{23}$$

which can be precomputed into a look-up table.

The performance of this FHT is illustrated by Fig. 2, which shows the evaluation of the Hankel transform

$$p(r,z) = \int_0^\infty \frac{e^{ik_z|z|}}{ik_z} kJ_0(kr)dk \tag{24}$$

representing the free-field point source field. $k_z = \sqrt{(\omega/c)^2 - k^2}$ is the vertical wave number at angular frequency ω. Figure 2(a) shows the FFP approximation which clearly breaks down at steep angles and short ranges, while Fig. 2(b) shows the correct spherical spreading behavior at all propagation angles produced using Eq. (21).

III. RESULTS

Using the FHT outlined in Eq. (21), Eq. (14) and its wave theoretic equivalent for scattering from density inhomogeneities[11] has been implemented inside the SAFARI/OASES[23] code in a numerically efficient way. In the algorithm, the code is first run to generate the incident field through the scattering volume, as indicated by the third line of Eq. (14). Under the Born Approximation this field is assumed to be unaffected by the scattering process. This incident field is then multiplied in the spatial domain with the azimuthally averaged scatterer distributions at each range and depth, as shown by the second line in Eq. (14). The resulting virtual source distribution at each scattering depth is then transformed to the scattered wave number domain. This gives the spectral distribution of the right-hand side of the inhomogeneous depth-separated wave equation for the scattered field. The source spectrum for the scattered field at each scatterer depth is essentially a more complicated version of a point source expansion, since there is now an array of point sources at each depth whose strengths depend both on the incident field and the distribution properties of the scatterers.

The resulting inhomogeneous depth separated wave equation for the scattered field is solved using the *Global Matrix* approach.[23] The result is the spatial distribution of the scattered field for the desired frequency. To generate scattered field time series, Eq. (14) must be solved over an array of frequencies for the same scatterer distribution. Thus the second line of Eq. (14) is evaluated once for the scatterer distribution and is then multiplied by the incident field at each frequency of interest at all wave numbers and depths in order to determine the virtual source representation. The resulting frequency dependent source term is then used to drive the depth separated wave equation for the scattered field, which is also frequency dependent, over the desired frequency band. The result is a complex transfer function between the incident field which was used to determine the third line of Eq. (14) and the scattered field at the desired horizontally monostatic receiver depths z.

The complex scattered field transfer functions may be used to synthesize scattered field time series using Fourier synthesis. The sampling requirements of the scattered field time series must be in harmony with those of the spatial sampling of the scatterer realization and the incident field. In practice the spatial integrals on the second and third lines of Eq. (14) are truncated at a range sufficient to give scattered returns from all times of interest in the temporal Fourier synthesis. For instance, for a 1 Hz sampling interval, scatterers up to a range of roughly 750 m are expected to contribute to the scattered field time series at the 1 s upper limit of the corresponding temporal window of the time series. Given a sample frequency of f_s the number of time samples is then $f_s/\Delta f$. In addition, the spatial sampling interval must be sufficiently fine to properly excite backscattered waves, which means that the maximum spatial sampling interval which is possible is one half a wavelength. Since the scatterer realization is generated once, this criteria is required to be satisfied at the upper end of the frequency band of interest. In practice the spatial sampling is also required to be smaller than the correlation length scale of the scatterers. The final requirement used was $\Delta x = 2\pi/k_{\max} \leqslant \min((\lambda/2),(\ell/10))$.

A. Scenario 1: Volume scattering from a slow sediment layer

Scattered field time series evaluated by Fourier synthesis of Eq. (14) have been generated for three scattering scenarios. Scenario 1 is illustrated in Fig. 3. A point source is situated 25 m above a slow sediment layer 100 m thick with a background sound speed of 1455 m/s, a background density of 1.024 g/cm^3, and an intrinsic attenuation of 0.01 dB/λ. In the sediment layer there is a distribution of sound speed and density fluctuations which are 100% correlated. The rms amplitude of the sound speed fluctuations is 1 m/s, while the rms density fluctuation is 7/1455 g/cm^3. The fluctuations are distributed according to a power law with a lateral correlation length scale $\ell_x = \ell_y = 10$ m and a vertical correlation length scale $\ell_z = 2$ m. These values are notional. Note that the relatively flat roll-off of the inhomogeneity spectrum ensures roughness in these realizations at a broad spectrum of spatial scales. The scatterer power spectrum required in Eq. (14) has the form

$$P_{\delta c}(p_r,p_z) = \langle \delta c^2 \rangle \frac{\ell_r^2 \ell_z \Gamma(1.75)}{\pi^{1.5}\Gamma(0.25)} \times (1 + p_r^2\ell_r^2 + p_z^2\ell_z^2)^{-1.75}, \tag{25}$$

which corresponds to a three-dimensional von Karman (as discussed by Turgut[13]) spectrum with fractal dimension 3.5.[24]

In all the scenarios, the properties of the basement are chosen to be identical to the background properties of the sediment layer. This is not a requirement of the implementation, which can indeed insert a volume scattering layer into an arbitrary horizontally stratified waveguide, but rather a choice which tends to make the benchmarking and explanation of the results more straightforward by eliminating multipath.

In Fig. 4 the absolute value of the complex envelope of the scattered field time series received on an array of receiv-

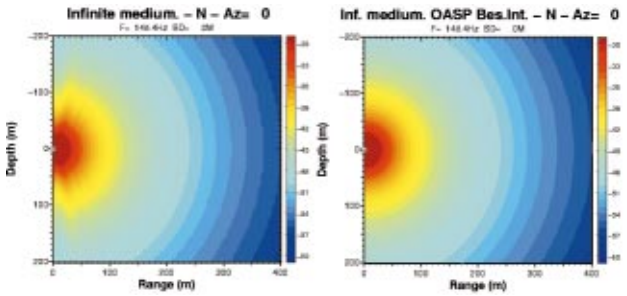

FIG. 2. Acoustic point source field. (a) shows the FFP approximation which clearly breaks down at steep angles and short ranges, while (b) shows the correct spherical spreading behavior at all propagation angles, produced using Eq. (21).

ers at the origin are shown in a stacked format for a particular realization of sediment inhomogeneities. The source pulse is Gaussian shaded

$$p_{\text{source}}(t,r=1\ \text{m}) = \exp\{-2i\pi f_o t - t^2 \Delta\omega^2/2\},$$

with a center frequency of $f_o = 500$ Hz and a bandwidth of $\Delta\omega/2\pi = 20$ Hz. The results show that the receivers closest to the sediment water interface receive the scattered field first, with the slope of the first arrival at higher receivers corresponding to the sound speed in the upper half space.

To further interpret the scattered field predictions it is useful to beamform the scattered field received on the vertical line array to transform the results to the time-angle domain. The resulting time-beam evolution of scattered field intensity, averaged over 16 independent scatterer realizations conforming to the distribution properties in Eq. (25), is shown in the lower panel of Fig. 5. In the upper panel an independent estimate of the beam-time evolution of backscatter intensity obtained with the ray trace code SCARAB[7,8] is

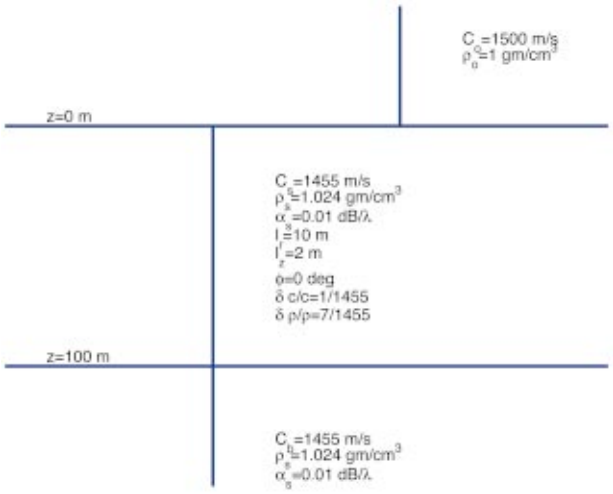

FIG. 3. Sound speed profile and scatterer properties of volume scattering Scenario 1. An isospeed halfspace overlies a slow sediment layer 100 m thick with a background sound speed of 1455 m/s and density of 1.024 g/cm^3. The basement halfspace has identical properties. In the scattering layer there are 100% correlated sound speed and density inhomogeneities conforming to a power law distribution with a fractal dimension of 3.5. The rms sound speed fluctuation is 1 m/s and the density fluctuation is 7/1455 g/cm^3. The horizontal correlation length scales of the scatterers is 10 m and the vertical correlation length scale is 2 m. The high frequency asymptote of the scatterer distribution power spectrum is $k^{-7/2}$.

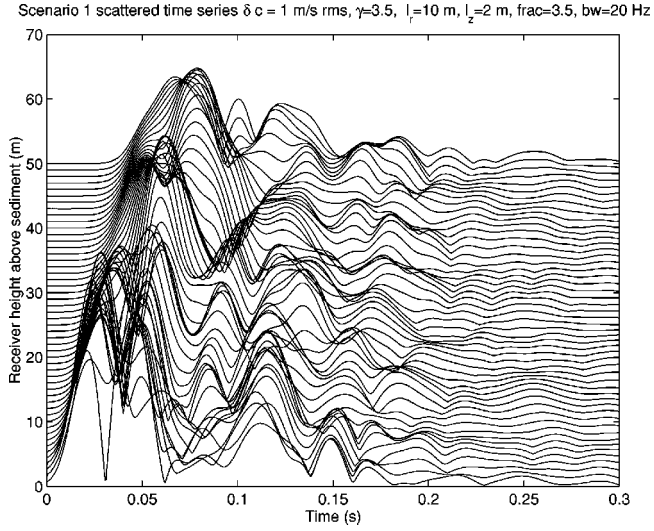

FIG. 4. Scenario 1 stacked scattered field time series. The absolute value of the complex envelope of the field received over a 50 m aperture array of receivers as a function of time after the source pulse. The source pulse is Gaussian shaded with a center frequency of 500 Hz and a bandwidth of 20 Hz.

shown for purpose of comparison. In the wave number integral representation the source pulse has a peak level of 1 μPa@1 m and is Gaussian shaded with a bandwidth of 20 Hz. In the SCARAB implementation the source pulse window is a rectangle of uniform amplitude of 1 μPa@1 m and duration $T = 5$ ms. The spectral results have therefore been adjusted to correct for the differences in incident energy between these two source pulses. The incident energy in the SCARAB source pulse is

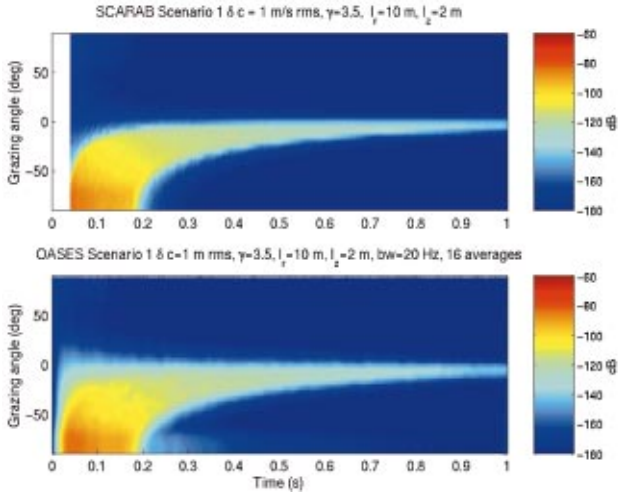

FIG. 5. The beam-time evolution of volume scattering intensity predicted by SCARAB (upper plot) and the wave number integral implementation discussed in this paper (lower plot). In the wave number integral approach, time series are collected and beamformed on an array with a 50 m aperture at the origin whose center is co-located at the source depth. The beamformed results are then squared and averaged over an ensemble of 16 independent realizations of the sediment inhomogeneities to give an estimate of the expected value of the scattered intensity. Good agreement is seen between the two approaches, with the scattered intensity falling between the time-angle trajectories of scatterers at the top and bottom of the sediment layer. Note that the beamforming of the wave number integral results introduces some sidelobes. The SCARAB results have no sidelobes because they are obtained directly in the time-angle domain.

$$E_{SCARAB} = \int_0^T \cos^2(i\omega_o t)\,dt = T/2 = 2.5E-3, \tag{26}$$

while for the wave number integral with the Gaussian shaded source pulse it is

$$E_{OASES} = \int_{-\infty}^{\infty} (\cos(i\omega_o t) e^{-(\omega-\omega_o)^2/2\Delta\omega^2})^2\,dt$$

$$= \sqrt{\pi}/2\Delta\omega = 1/80\sqrt{\pi}. \tag{27}$$

With the normalization of the scattered pressure computed by the wave number integral technique by the factor $\sqrt{0.2\sqrt{\pi}}$ it is possible to directly compare the scattered field intensity received by a single hydrophone with the SCARAB predictions. The results are shown in Fig. 6 for a receiver at the source depth of 25 m above the sediment-water interface. In general the agreement between the two results is quite good, within 1 or 2 dB over the range of times and angles.

The agreement between the wavenumber integral and SCARAB representations of the scattered field intensity is satisfying because the differences between Eq. (14) and the sonar type equation for RL in the SCARAB manual are quite significant (for convenience, a short description of the SCARAB model is given in the Appendix). While both models use the Born Approximation and first order perturbation theory, both the Green functions and the scattering are treated differently in practice. SCARAB has a ray trace approximation for the Green function, while the wave number integral implementation accurately models the total Green function, including evanescent waves, turning points, and propagation near the critical angle for fast bottoms. For scattering SCARAB integrates the differential plane wave scattering cross-section of the sediment inhomogeneities over the sediment volume to estimate the scattered intensity, while the wave number integral calculates the scattered pressure from each scatterer over a particular realization of scatterers. In the case of wave number integral results, the expected value of the scattered intensity must be estimated by Monte Carlo averaging the square of the scattered pressure over an ensemble of scatterer realizations.[25] Finally, the expression SCARAB uses for the differential cross-section, Eq. (42) from Yamamoto,[6] also does not require the gradient of the scatterer distribution or of the incident field, as do the density scattering contributions in the wave number integral representation.[11] Thus good agreement between the SCARAB and the wave number integral results lends confidence that Eq. (14) and the numerical implementation are consistent with the sonar equation approach to describing the sediment inhomogeneity scattering process for slow bottoms. As discussed below, we expect the two approaches to be equivalent only in cases where the sediment scattering process is well described by a plane wave differential scattering cross section and where the propagation is well approximated by ray theory.

B. Scenario 2: Volume scattering from a fast sediment layer

One significant advantage of using the wave number integral approach to modeling sediment volume inhomogeneity scattering is that the Green function is accurately modeled. Failings in the ray theory approximation to the Green functions are especially evident near turning points in refractive sediments and near the critical angle for fast sediments. Another significant advantage is that the wave number integral approach correctly includes the scattering response of scatterers which have been excited by evanescent, or nonpropagating waves. This type of scattering is typically found in fast sediments along the sediment water interface at ranges where the incident angle of the source is smaller that the critical angle. For scatterers ensonified by these types of waves, the differential plane wave scattering cross section is undefined. Yet it is known that scatterers ensonified by these types of waves can be important contributors to the total scattered field.[9] In fact sub-critical penetration and scattering is the basis for advanced mine hunting sonar concepts for buried object detection.[26,27] If this mechanism is going to be included for modeling target response, it is important that a similar mechanism be included for modeling the reverberation from sediment volume inhomogeneities, especially for smooth bottoms. For these reasons in Scenario 2 we compare the scattering predictions of the wave number integral approach to SCARAB for a fast sediment scattering scenario in order to evaluate the differences between the two approaches when there is a critical angle.

Scenario 2 is illustrated in Fig. 7. A point source is situated 25 m above a fast sediment layer 100 m thick with a background sound speed of 1600 m/s, density of 2 g/cm^3, and attenuation of 0.01 dB/λ. In the sediment layer there is the similar distribution of 100% correlated sound speed and density fluctuations as were described in Scenario 1. The rms sound speed fluctuation is 1 m/s, the rms density fluctuation is 7/1600 g/cm^3, and the correlation length scales are $\ell_x = \ell_y = 10$ m and $\ell_z = 2$ m. The source characteristics are the same as in Scenario 1.

In Fig. 8 the time-angle evolution of backscattered intensity is illustrated for the fast sandy bottom type of Scenario 2. The SCARAB result is shown in the top plot and the wavenumber integral result is shown in the bottom plot. The results are in good agreement for angles greater than the critical angle of 20°, but the wave number integral result also shows a shallower angle branch at late time which conforms to the time-angle trajectory of the sediment water interface. This upper trace corresponds to the inhomogeneous forcing of scatterers by nonpropagating evanescent waves at the sediment water interface. Since the waves are not propagating in the sediment, there is no differential scattering cross section for SCARAB to use to estimate this branch. Instead SCARAB estimates that the only propagation path of importance to scatterers near the sediment water interface is the headwave path, which enters the sediment at the critical angle and propagates at near-horizontal angles to these scatterers and back. This is a fundamental limitation of the SCARAB assumption that all of the scattering of the sediment volume inhomogeneities can be parameterized in terms of differential scattering cross section.

In Fig. 9 the scattered intensity received monostatically for Scenario 2 is illustrated in red. Here it is seen that although the SCARAB result neglects the inhomogeneous scat-

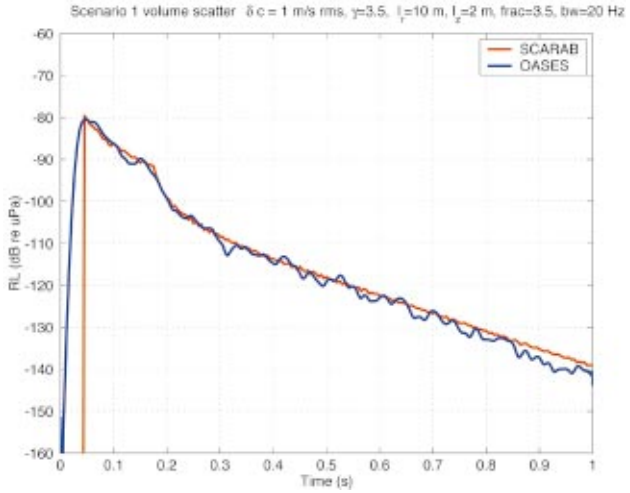

FIG. 6. Single phone scattered field intensity estimates from SCARAB (red) and the current implementation (blue). The wave number integral estimates of the scattered pressure have been squared and averaged over 16 independent realizations of the sediment layer inhomogeneities. Agreement with the SCARAB results is quite good, typically within 1 or 2 dB.

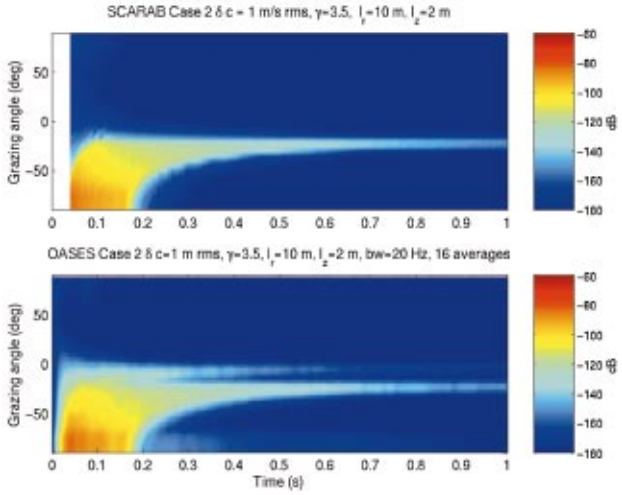

FIG. 8. The time-beam evolution of scattered intensity for Scenario 2. While the general agreement at angles greater than the critical angle is very good, the forced evanescent scattering branch following the time-angle trajectory of the sediment-water interface is missing in the SCARAB result (top). This branch is seen in the wave number integral results (bottom) as well as the headwave scattering branch arriving at and above the critical angle of 20°. The presence of the fast sediment causes the scattering associated with the propagating part of the Green function to be confined to angles greater than or equal to the critical angle of the bottom for all times greater that the time necessary to interrogate the sediment layer at the critical angle, about 90 ms for the current geometry.

tering mechanism, the overall agreement between the wave number integral result and SCARAB is still good. This is because in this case the attenuation in the sediment, 0.01 dB/λ, is sufficiently small that the headwave propagation path is the strongest contributor to the total scattered field for the times of interest in this simulation. However, in Scenario 2a when we increase the sediment attenuation to 0.5 dB/λ, the blue curves show that SCARAB and the wave number integral result no longer agree for times later than about 0.16 s. This is due to the lack of an evanescent scattering mechanism in SCARAB. Taken together, the results for Scenarios 2 and 2a indicate that the evanescent scattering mechanism is about 20 dB down from the headwave mechanism in the absence of loss. For the sake of completeness, the beam time trajectories for Scenarios 2 and 2a are illustrated in Fig. 10.

C. Scenario 3: Volume scattering from an upward refracting sediment layer

Gradients in the background properties of sediments are commonly observed in coring data and in bottom sound speed inversions.[28,29] Gradients are important to the physics of the scattering process because they control how the subbottom is illuminated.[4,8] These gradients are often composed of microstructure with significant sound speed and density variance. However, some of the characteristics of scattering from these types of sediments may be accounted for by assuming that the background properties are smoothly varying

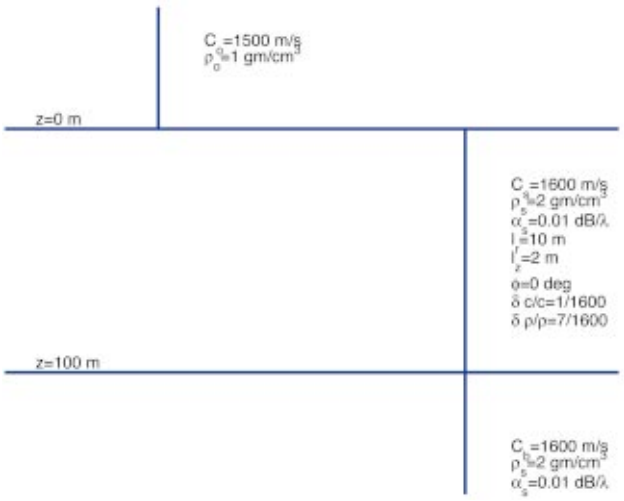

FIG. 7. Scenario 2 is typical of a sandy sediment layer, with a sediment background sound speed of 1600 m/s, density of 2 g/cm^3, and attenuation of 0.01 dB/λ. The basement properties are identical to the background properties of the sediment, and the scatterer distribution properties are identical to those in Scenario 1.

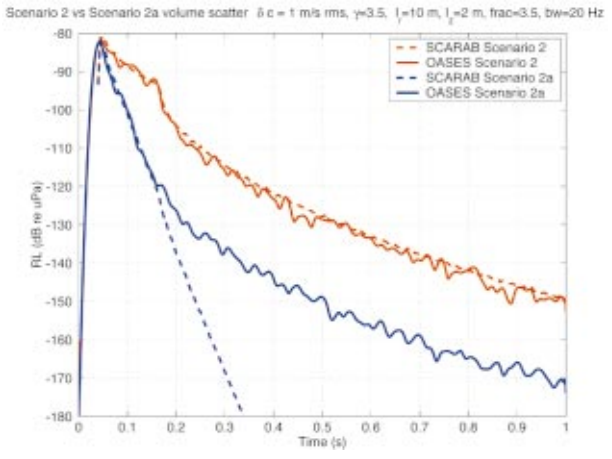

FIG. 9. Single phone average intensity estimates for Scenario 2 (red) and Scenario 2a (blue) which has a higher sediment attenuation of 0.5 dB/λ. The equivalent SCARAB predictions are indicated by the dashed lines of the appropriate color. The results show that in Scenario 2a the SCARAB and wave number integral results do not agree. This is due to the absence in SCARAB of an evanescent wave scattering mechanism.

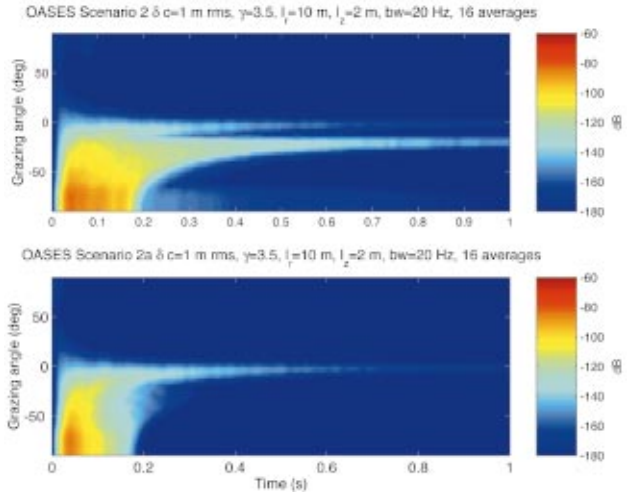

FIG. 10. The time-beam evolution of scattered intensity for Scenario 2 (upper panel) and Scenario 2a (lower panel) which has a lossier sediment. In the lossier sediment case, the headwave scattering branch is attenuated after about 0.3 s. At times greater than this, the evanescent scattering path associated with the sediment water interface is the only scattering mechanism of importance.

over the depth of the sediment layer. In wave number integral techniques, sound speed gradients which obey linearity in the square of the index of refraction may be handled exactly, as in these cases the depth separated wave equation becomes a differential equation whose solutions are Airy functions.[4,16] In Scenario 3 such a gradient is introduced into the background sound speed properties of the fast sandy sediment in Scenario 2 (Fig. 11). The sound speed at the bottom of the layer is increased to 1700 m/s, while all the other properties of the sediment layer are held fixed. To eliminate multipath, the basement sound speed is also set at 1700 m/s.

The effect of the sound speed gradient on the incident field is illustrated in Fig. 12, where the range-depth transmission loss is shown for the point source 25 m above the sediment water interface at 500 Hz for Scenarios 2 and 3. In both scenarios, the incident field passes unhindered into the sediment layer save for a small reflection loss for ranges up to 67 m, where the critical angle occurs. However in Scenario 2, the field then passes down into the lower halfspace, while in Scenario 3 a significant portion of the transmitted energy is refracted back up into the sediment layer.

In Fig. 13 the time angle distributions of backscattered intensity for Scenarios 2 and 3 are shown. The results show that these distributions are significantly different. While the high angle early time backscatter and the forced inhomogeneous backscatter associated with the sediment water interface are identical for the two scenarios, the deep refracted or headwave path contains significantly more energy at late time for Scenario 3 than it does for Scenario 2. The angular width of the refracted scattering branch is also wider for Scenario 3, because higher angle energy is able to ensonify the sediment layer at late times due to the refraction of this energy back into the sediment layer before it can escape into the basement.

In Fig. 14 the backscattered intensity for the two scenarios is shown. Here it can be seen that the decay rate of the

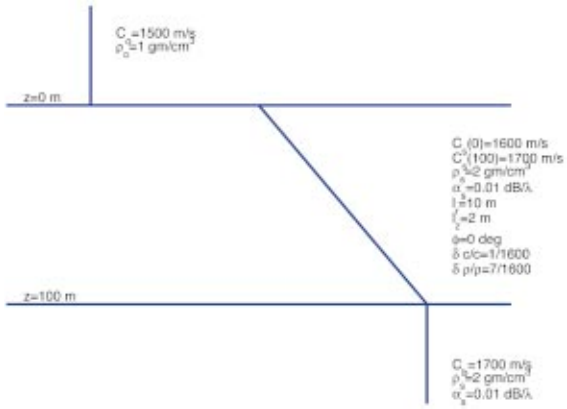

FIG. 11. Scenario 3 is an upward refracting sandy sediment layer, with a sediment background sound speed of 1600 m/s at the sediment water interface, 1700 m/s at the sediment-basement interface, density of 2 g/cm^3, and attenuation of 0.01 dB/λ. The basement has a sound speed of 1700 m/s and has properties which are otherwise identical to those of the sediment layer. The scatterer distribution in the sediment layer are identical to those in Scenario 2.

reverberation from the sediment volume inhomogeneities in the upward refracting sediment in Scenario 3 is significantly slower that for the iso-speed sediment in Scenario 2. The implication is that sediment gradients can have a very significant effect on both the levels and the decay characteristics of sediment scattering.

IV. CONCLUSIONS

The wave number integral representation for monostatic backscatter from three-dimensional sediment inhomogene-

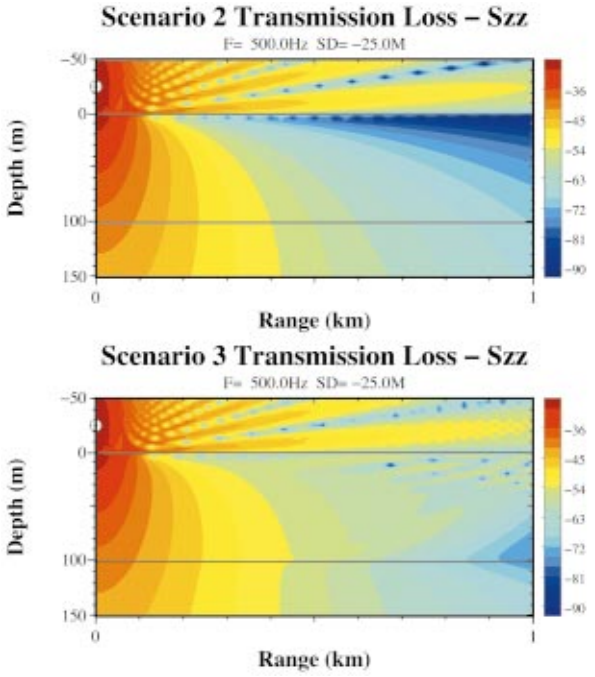

FIG. 12. The range-depth transmission loss for Scenarios 2 (top) and 3 (bottom) at 500 Hz. In Scenario 2 the energy passing into the bottom above the critical angle passes through the sediment basement interface and is lost to the sediment layer. In Scenario 3 the upward refracting sediment sound speed causes a significant amount of the incident energy to be retained at longer ranges from the source.

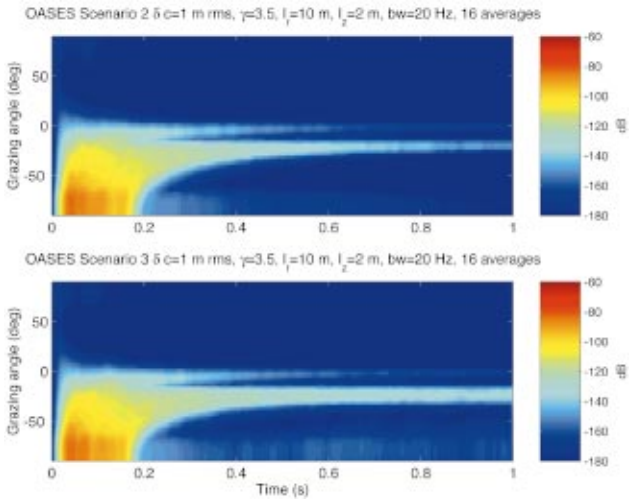

FIG. 13. Time-angle evolution of scattered intensity for the iso-speed fast bottom in Scenario 2 (upper plot) and the upward refracting sediment in Scenario 3 (lower plot). The results for Scenario 3 indicate that upward refracting sediments can have significantly more late time reverberation over a broader range of grazing angles than otherwise similar sediment layers without gradients.

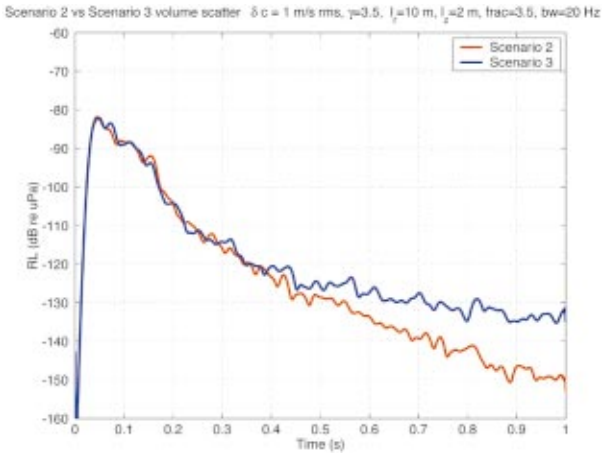

FIG. 14. The scattered intensity received in a monostatic configuration for a fast sediment without a sound speed gradient (Scenario 2, red curve), and a fast upward refracting sediment (Scenario 3, blue curve). The results indicate that sediment gradients can have a very significant effect on scattered levels from sediment volume inhomogeneities at late time.

ities has been derived using the method of small perturbations and the Born Approximation, and these equations have been implemented in a computationally efficient manner. The code offers the capability for evaluating Monte Carlo estimates of backscattered intensity and the time-angle evolution of backscattered intensity for isotropic, horizontally stratified sediment scenarios with critical angles and turning points where the scatterers are treated using the perturbation and single scattering approximations. The potential also exists for treating sediment volume inhomogeneity scattering in more complicated horizontally stratified bottoms by superimposing the single layer results derived and implemented here for all the contributing layers. For single layers, the results obtained here indicate that for slow sediments, the wave number integral estimates of backscattered intensity are in excellent agreement with those obtained by SCARAB using a simple sonar equation approach, as expected. However for fast and upward refracting sediments, the complete first order perturbation solution for the scattered field can only be obtained through the use of the wave number integral approach.

For fast sediments, it is found that a second scattering branch exists in the time-angle plane of scattered intensity. This second branch follows the time-angle evolution of scattering from the sediment-water interface, and is associated with the inhomogeneous excitation of the volume inhomogeneity scatterers closest to the sediment water interface. Since these scatterers are ensonified by nonpropagating waves, they have no defined farfield scattering cross section. Yet the results show that these scatterers can and do contribute to the backscattered signal in an important way. For inhomogeneities in fast smooth sediments with significant attenuation, this scattering mechanism is the only contributor to reverberation at late time.

For upward refracting sediments, it is shown that the intensification of the incident field on sediment inhomogeneities beyond the turning point of the basement grazing rays leads to increased backscattered levels at late time. This phenomenon is most likely to be observable in weakly lossy sediments, and is accurately modeled near ray caustics with the wave theoretic approach used here.

The numerical implementation of a benchmarked wave number integral formalism for three-dimensional sediment inhomogeneity scattering into the SAFARI/OASES framework makes it possible to evaluate the quality of the various approximations which are routinely taken for perturbation estimates of backscattered intensity from sediments. In this paper we have concentrated on evaluating the suitability of using approximate Green functions, but the code also can be used to evaluate the suitability of assuming that the vertical correlation length scale of the bottom inhomogeneities is infinitesimal.

ACKNOWLEDGMENTS

The authors wish to acknowledge Charles Holland, Peter Neumann, and Andrew Rogers for supplying the SCARAB code and Ivar Bratberg for his assistance modifying and running it. The MIT part of this work was funded by the Office of Naval Research, Ocean Acoustics Program.

APPENDIX: EXPRESSIONS FOR SCATTERED INTENSITY USED BY SCARAB

The SCARAB model was developed to address deficiencies of many of the then existing bottom scattering models. Holland and Neumann[8] departed from the commonly used local plane-wave approximation (which they showed was inadequate) by modeling the received level in the time domain with all of the experiment complexities, then calculated bottom scatter under exactly the same assumptions as the measured data were processed. This is the essence of the SCARAB model: to model as closely as possible the measurement conditions, including assumptions used in the data processing.

Invoking the Born Approximation, the received level from a single ping can be written as a sum of delayed, scaled, replicas of the transmit source intensity $S(t)$:

$$RL(T,\theta) = 10\log\left[\sum_{i=1}^{N} S(t-t_i)10^{TL_i^1/10} \times 10^{-TL_i^2/10}\frac{dP}{d\Omega}(\theta_i, z_i)\right], \quad \text{(A1)}$$

where TL_i^1 and TL_i^2 are the transmission losses (including the beam pattern) from the source to scattering element i and from element i back to the receiver respectively. For subbottom volume scattering $dP/d\Omega$ is the differential scattering cross-section of a scatterer i at depth z; N is the number of scatterers. In the initial version of the model used in Ref. 8, the propagation to and from the scatterers was computed using OASES and the scattering was calculated from randomly distributed 3-D ellipsoids. A later version of the model employs a number of simplifications including use of ray theory for the propagation and replacing the scattering from randomly distributed deterministic scatterers with a stochastic approach.[7] It is this simple version of the model that is used in the comparisons in this paper.

[1] A. N. Ivakin and Y. P. Lysanov, "Theory of underwater sound scattering by random inhomogeneities of the bottom," Sov. Phys. Acoust. **27**, 61–64 (1981).
[2] A. N. Ivakin, "A unified approach to volume and roughness scattering," J. Acoust. Soc. Am. **103**, 827–837 (1998).
[3] D. Tang, "Acoustic Wave Scattering from a Random Ocean Bottom," Doctoral Dissertation, MIT-WHOI Joint Program, WHOI-91-25, June 1991.
[4] P. D. Mourad and D. R. Jackson, "A model/data comparison for low frequency bottom backscatter," J. Acoust. Soc. Am. **94**, 344–358 (1993).
[5] B. H. Tracey and H. Schmidt, "A self-consistent theory for seabed volume scatter," J. Acoust. Soc. Am. **106**, 2524–2534 (1999).
[6] T. Yamamoto, "Acoustic scattering in the ocean from velocity and density fluctuations in the sediments," J. Acoust. Soc. Am. **99**, 866–879 (1996).
[7] A. Rogers and C. Holland, "SCARAB version 1.01, Users Manual," August 1997, Planning Systems Incorporated.
[8] C. W. Holland and P. Neumann, "Sub-bottom scattering: A modeling approach," J. Acoust. Soc. Am. **104**, 1363–1373 (1998).
[9] P. C. Hines, "Theoretical model of acoustic backscatter from a smooth seabed," J. Acoust. Soc. Am. **88**, 324–334 (1990).
[10] P. C. Hines, "Theoretical model of in-plane scatter from a smooth sediment seabed," J. Acoust. Soc. Am. **99**, 836–844 (1996).
[11] K. D. LePage and H. Schmidt, "Spectral integral representations of volume scattering in sediments in layered waveguides," J. Acoust. Soc. Am. **108**, 1557–1567 (2000).
[12] H. Schmidt and K. D. LePage, "Spectral integral representations of multistatic scattering from sediment volume inhomogeneities," J. Acoust. Soc. Am. **108**, 2564 (2000).
[13] A. Turgut, "Inversion of bottom/subbottom statistical parameters from acoustic backscatter data," J. Acoust. Soc. Am. **102**, 833–852 (1997).
[14] H. Schmidt and J. Lee, "Physics of 3-D scattering from rippled seabeds and buried targets in shallow water," J. Acoust. Soc. Am. **105**, 1605–1617 (1999).
[15] H. Schmidt and J. Glattetre, "A fast field model for three-dimensional wave propagation in stratified environments based on the global matrix method," J. Acoust. Soc. Am. **78**, 2105–2114 (1985).
[16] F. B. Jensen, W. A. Kuperman, M. B. Porter, and H. Schmidt, Eq. 4.93, *Computational Ocean Acoustics* (Springer-Verlag, New York, 2000).
[17] F. B. Jensen, W. A. Kuperman, M. B. Porter, and H. Schmidt, Eq. 2.103, *Computational Ocean Acoustics* (Springer-Verlag, New York, 2000).
[18] F. DiNapoli and R. Deavenport, "Theoretical and numerical Green's function solution in a plane multilayered medium," J. Acoust. Soc. Am. **67**, 92–105 (1980).
[19] J. A. Ferrari, D. Perciante, and A. Dubra, "Fast Hankel transform of nth order," J. Opt. Soc. Am. A **16**, 2581–2582 (1999).
[20] Q. H. Liu and W. C. Chew, "Applications of the conjugate gradient fast Fourier Hankel transfer method with an improved fast Hankel transform algorithm," Radio Sci. **29**, 1009–1022 (1994).
[21] Q. H. Liu and Z. Q. Zhang, "Nonuniform fast Hankel transform (NUFHT) algorithm," Appl. Opt. **38**, 6705–6708 (1999).
[22] M. Abramowitz and I. A. Stegun, *Handbook of Mathematical Functions* (Dover, New York, 1970).
[23] H. Schmidt, "SAFARI: Seismo-acoustic fast field algorithm for range independent environments. User's Guide," SR-113, SACLANT Undersea Research Centre, La Spezia, Italy (1988) (AD A 200 581).
[24] J. A. Goff and T. H. Jordan, "Stochastic modeling of seafloor morphology: Inversion of sea beam data for second order statistics," J. Geophys. Res. **93**, 13589–13608 (1988).
[25] W. H. Press, B. P. Flannery, S. A. Teukolsky, and W. T. Vetterling, *Numerical Recipes in C* (Cambridge University Press, Cambridge, 1988).
[26] A. Maguer, W. L. J. Fox, H. Schmidt, E. Pouliquen, and E. Bovio, "Mechanisms for subcritical penetration into a sandy bottom: Experimental and modeling results," J. Acoust. Soc. Am. **107**, 1215–1225 (2000).
[27] A. Maguer, E. Bovio, W. L. J. Fox, and H. Schmidt, "*In situ* estimation of sediment sound speed and critical angle," J. Acoust. Soc. Am. **108**, 987–996 (2000).
[28] C. W. Holland and J. Osler, "High resolution geoacoustic inversion in shallow water: A joint time and frequency domain technique," J. Acoust. Soc. Am. **107**, 1263–1279 (2000).
[29] C. W. Holland, R. Hollett, and L. Troiano, "Measurement technique for bottom scattering in shallow water," J. Acoust. Soc. Am. **108**, 997–1011 (2000).